International Journal of Nanomedicine

Dovepress
Taylor & Francis Group

Open Access Full Text Article

ORIGINAL RESEARCH

NIR Triggered Bionic Bilayer Membrane-Encapsulated Nanoparticles for Synergistic Photodynamic, Photothermal and Chemotherapy of Cervical Cancer

Jiayi Ding[1], Xueliang Zhang[2], Le Guo[1], Jiabao Xiong[3], Chi Zhang[1], Zhong Du[3], Lijun Zhu[3], Nuernisha Alifu[1–3], Biao Dong[2,4]

[1]Institute of Public Health, Xinjiang Medical University, Urumqi, 830011, People's Republic of China; [2]State Key Laboratory of Pathogenesis Prevention and Treatment of High Incidence Diseases in Central Asia, School of Medical Engineering and Technology Xinjiang Medical University, Urumqi, 830011, People's Republic of China; [3]Second Clinical Medical College, Xinjiang Medical University, Urumqi, 830011, People's Republic of China; [4]State Key Laboratory on Integrated Optoelectronics, College of Electronic Science and Engineering, Jilin University, Changchun, 130012, People's Republic of China

Correspondence: Nuernisha Alifu, State Key Laboratory of Pathogenesis Prevention and Treatment of High Incidence Diseases in Central Asia, School of Medical Engineering and Technology Xinjiang Medical University, Urumqi, 830011, People's Republic of China, Tel +86-18799167931, Email nens_xjmu@126.com; Biao Dong, State Key Laboratory on Integrated Optoelectronics, College of Electronic Science and Engineering, Jilin University, Changchun, 130012, People's Republic of China, Tel +86-13504329842, Email dongb@jlu.edu.cn

Purpose: A synergistic treatment strategy of phototherapy and chemotherapy has been shown to improve efficacy and offer unique advantages over monotherapy. The purpose of this study is to explore a new nanocarrier system with liposome as the inner membrane and erythrocyte membrane as the outer membrane, which aims to realize the leak-free load of phototherapy drug indocyanine green (ICG) and chemotherapy drug doxorubicin (DOX), prolong the circulation time in vivo and improve the therapeutic effect.

Patients and Methods: In this study, bilayer membrane-loaded ICG and DOX nanoparticles (RBC@ICG-DOX NPs) were prepared and characterized. For in vitro analysis, the biocompatibility and tumor inhibition properties of the nanoparticles were evaluated. For in vivo analysis, the antitumor properties of the nanoparticles were explored in a mouse subcutaneous tumor model.

Results: RBC@ICG-DOX NPs were successfully prepared with strong safety and good blood compatibility, which can effectively reduce drug leakage and prolong drug circulation time in the body. In vitro performance evaluation showed that RBC@ICG-DOX NPs obtained excellent photothermal conversion ability and well reactive oxygen generation performance under near-infrared laser irradiation. Both in vitro and in vivo experiments showed well phototherapy-chemotherapy effect of RBC@ICG-DOX NPs with low toxic side effects.

Conclusion: Drug delivery, imaging and tumor synergies were accomplished through combinatorial strategies as well as bilayer membrane encapsulation, opening up a new platform for the design of future tumor combination therapies.

Keywords: erythrocyte membrane modification, indocyanine green, adriamycin, combination therapy, cervical cancer

Introduction

With the development of optical technologies, phototherapy, which simultaneously provides light-induced diagnosis, imaging, and treatment, has received increasing attention in the field of oncology.[1,2] Near-infrared (NIR) light in the wavelength range of 780–1700 nm obtains the characteristics of deep tissue penetration, low damage to normal cells, low autofluorescence, and low light scattering,[3,4] which has been regarded as a transparent therapeutic window for in vivo light-activated drug delivery systems,[5–7] thus providing remarkable conditions for tumor imaging and treatment. As an emerging therapeutic modality, phototherapy, which mainly includes photodynamic therapy (PDT) and photothermal therapy (PTT), has garnered extensive research attention because of its safe and non-invasive nature. By utilizing NIR light guidance, phototherapy converts light energy into chemical or thermal energy, which destroys target cells while reducing toxicity to normal tissues.[8] Additionally, the localized thermal effect of PTT accelerates the blood flow rate, thereby increasing the oxygen supply and enhancing the efficacy of PDT, suggesting a synergistic effect of PTT and

Received: 16 October 2024
Accepted: 10 December 2024
Published: 6 January 2025

PDT.[9] ICG and its derivatives have been reported to exhibit both PDT and PTT effects, demonstrating significant absorption in the NIR region. Consequently, several studies have employed ICG or its derivatives for combination antitumor therapies.[10]

The combination of nanotechnology-based phototherapy and chemotherapy is currently considered a promising treatment option.[11,12] In preclinical animal investigations, synergistic phototherapy-chemotherapy in particular has been proven to increase treatment efficacy, decrease negative side effects, and offer special benefits above traditional chemotherapy.[13–15] Thermotherapy has demonstrated the ability to enhance intratumoral permeability, facilitate the transport of therapeutic agents within tumors, and modulate the permeability of local vascular and cellular membranes. This process results in increased brittleness of tumor cells, thereby augmenting their sensitivity to therapeutic drugs.[16] Chen et al designed a drug delivery system (AuNRs@DOX) to attach adriamycin (DOX) to the surface of gold nanorods for combined photothermal and chemotherapeutic treatments of cancer. AuNRs@DOX significantly enhances adriamycin cytotoxicity through the photothermal effect under NIR laser light of 808 nm and induces an increase in the apoptosis of the tumor cells, leading to a better therapeutic in vitro and in vivo effect.[17] Furthermore, thermotherapy causes the temperature to rise while causing the thermal response system to release medications quickly.[18] The mechanisms of combined phototherapy and chemotherapy are complex. Beyond the direct damage caused by these treatment modalities, their effects on the tumor vascular system and the induction of immune responses also contribute to synergistic antitumor therapy.[10] Specifically, phototherapy can permeabilize the tumor vascular system, enhancing drug delivery and increasing tumor cell sensitivity to chemotherapeutic agents. Conversely, chemotherapy can improve the efficacy of phototherapy by targeting surviving cancer cells or inhibiting the regeneration of damaged tumor vasculature.[19] Light-based therapies combined with chemotherapy have more satisfactory efficacy and maximize therapeutic outcomes compared to their respective monotherapies.[20] However, the toxic side effects of the broad-spectrum chemotherapeutic drug adriamycin (DOX) have limited its clinical application. Additionally, a significant challenge remains in loading both therapeutic agents simultaneously in a way that enhances their therapeutic efficacy, safety, and blood circulation time.

In recent years, researchers have developed various nanodelivery platforms to improve the solubility or stability of therapeutic drugs, thereby improving their bioavailability.[21,22] Compared with small molecules alone, nanocarriers offer unique physicochemical properties that enable them to penetrate or cross biological barriers. They also achieve extended blood circulation time and high synergistic efficiency through straightforward chemical modification.[23,24] Liposomes are one of the most studied nanocarriers and have been successfully used in clinical cancer therapy.[25,26] However, the instability of liposomes, their low tolerance to gastric acid pH, and their clearance from the bloodstream by the mononuclear phagocytosis system—as foreign bodies, despite their close resemblance to biological membranes—have limited their effectiveness in prolonging drug survival time and reducing toxicity.[27] In addition, liposome-carried drugs may leak in the circulation before reaching the tumor site. Premature drug release not only reduces the amount of drug reaching the tumor site but also increases damage to normal tissues.[28,29] Biomimetic strategies using natural cell membrane-modified nanoparticles have attracted attention due to their inherent biocompatibility, biodegradability, and nonimmunogenic properties.[30,31] Based on the characteristics and functions of different cells, composite nanomaterials with various cell membrane modifications can be designed. This approach is akin to using cell membranes to create simulated cells, enabling prolonged blood circulation in the body while retaining the inherent functions of the cell membranes. Currently, a range of cell membranes (red blood cell membranes,[32] platelet membranes,[33] tumor cell membranes[34] and macrophage membranes[35]) have been selected for the preparation and development of membrane-modified nanosystems. Erythrocyte (red blood cell, RBC) membranes are recognized as the most abundant and convenient biocarriers for tumor drug delivery systems. This is attributed to their ability to effectively reduce phagocytosis by macrophages, prolong circulation time in the bloodstream, and exhibit inherent biocompatibility and biodegradability. These characteristics contribute to improved nanoparticle stability, enhanced storage duration in vitro, and reduced aggregation. Additionally, the absence of nuclei and complex organelles in mature erythrocytes facilitates easy extraction.[36,37] Therefore, utilizing erythrocyte membranes for the surface modification of nanoparticles may enhance the stability of drug delivery systems and extend their circulation times in vivo.

In this work, we propose a bilayer bionic membrane modification strategy that modifies the erythrocyte membrane on liposomes. Bilayer membrane nanocarriers were used to load NIR light-triggered ICG molecules and the chemotherapeutic

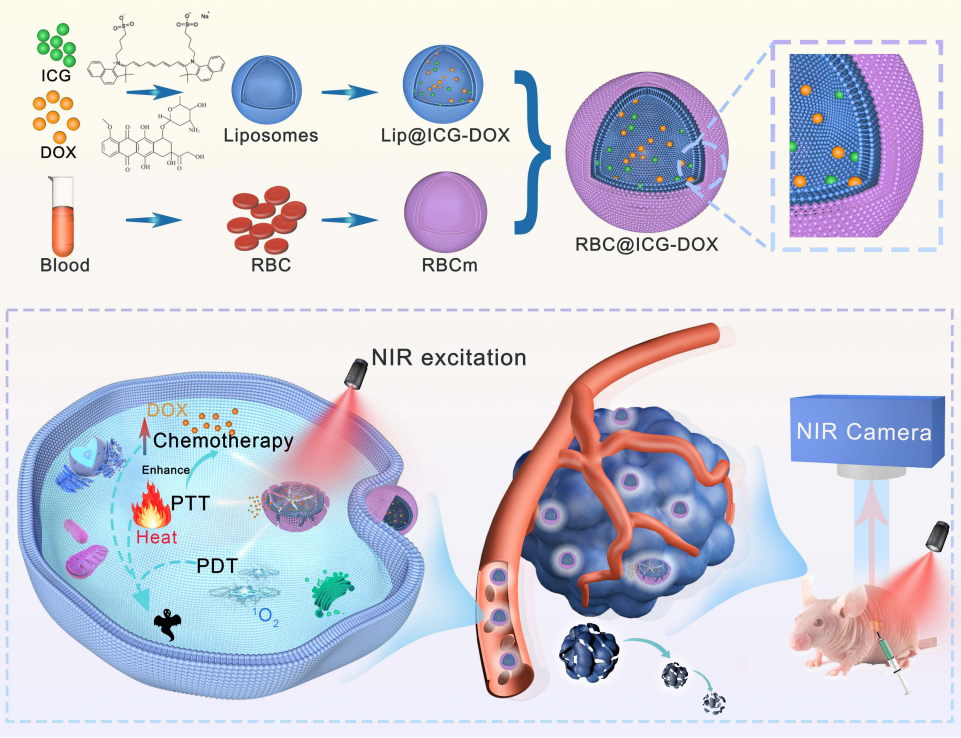

Scheme 1 Synthesis process of RBC@ICG-DOX NPs and schematic diagram of PDT, PTT and chemotherapy synergistic treatment.

drug DOX, forming RBC@ICG-DOX nanoparticles (NPs). In this design, besides DOX, all other components are highly biocompatible. The bilayer membrane design can provide great DOX leakage protection during blood circulation. Utilizing the NIR fluorescence properties of ICG, the position of the bilayer membrane carrier probe can be monitored. Additionally, its PTT function enables controlled DOX release, and its PDT function can further achieve synergistic therapeutic effects (Scheme 1). Systematic in vitro and in vivo experiments showed that RBC@ICG-DOX NPs can effectively generate ROS, photothermal, and chemotherapeutic effects, thereby improving tumor killing efficiency. This synergistic approach, which combined PDT, PTT and chemotherapy, provides a promising strategy for cancer treatment.

Materials and Methods

Materials and Instruments

Indocyanine green and adriamycin were purchased from Beijing Inokai Technology Co., Ltd. (China). Distearoyl phosphatidylethanolamine-polyethylene glycol 2000 (DSPE-PEG_{2000}), cholesterol (chol), and lecithin were purchased from Xi'an Ruixi Biological Technology Co., Ltd. (China). Polycarbonate membrane was purchased from Whatman (Shanghai, Beijing). 9,10-Anthracenediyl-bis (methylene) malonic acid (ABDA), and 2,7-dichlorodihydrofluorescein diacetate (DCFH-DA) were purchased from Shanghai Aladdin Biochemical Technology Co., Ltd. (China). Fetal bovine serum (FBS) was purchased from Shanghai Thermo-Fisher Scientific Co., Ltd. (China). High-sugar (DMEM), phosphate-buffered salt solution (PBS) was purchased from Beijing Wobisen Technology Co., Ltd. (China). Hoechst 33342 and enhanced cell counting kit-8 (CCK-8) were obtained from Beijing Solarbio Science & Technology Co., Ltd. (China). All the experimental procedures were performed using deionized (DI) water.

The morphology and size of the NPs were observed by transmission electron microscopy (TEM, FEI, TF 20, USA). Particle size distribution was measured by dynamic light scattering analysis (Brookhaven, NanoBrook 90plus PALS, USA). Absorption and fluorescence spectra were recorded by a Shimadzu UV-3600i Plus spectrophotometer (Japan) and a Shimadzu RF-6000 spectro fluorophotometer (Japan). NIR fluorescence microimaging was performed using a confocal laser scanning microscope (CLSM, NIKON AXR Laser Confocal Microscope, Japan). Apoptosis rate was detected using flow cytometry (BD, LSR II, USA).

https://doi.org/10.2147/IJN.S496982

Preparation of RBC@ICG-DOX NPs

RBC@ICG-DOX NPs were synthesized as follows.[38–40] Lecithin, cholesterol, DSPE-PEG_{2000} and ICG were taken and dissolved in a certain proportion, and put into 3 mL of chloroform by rotary evaporation to form a film. Then, 1 mL of adriamycin solution (1 mg mL^{-1}) was added into the mixture. Next, it was subjected to ultrasound and liposome extruder treatment to form liposome-coated ICG-DOX (Lipo@ICG-DOX NPs).[41,42] Dialysis was performed to remove unloaded ICG and DOX, and then supplemented with 5 mL of DI water. Erythrocytes were obtained by centrifugation (4000 rpm, 10 min) of whole blood of mouse and washed three times with cold 1× PBS.[43] Erythrocyte membranes were collected by lysing the erythrocytes with 0.1 × PBS and centrifuging at 8000 rpm for 5 min to remove hemoglobin. The prepared liposomes encapsulated ICG-DOX were mixed with erythrocyte membranes, and the mixtures were extruded 10 times through polycarbonate membranes with pore sizes of 200 and 100 nm, respectively.

Characterization of RBC@ICG-DOX NPs

The morphology of the RBC@ICG-DOX NPs was characterized by TEM method. The average particle size and zeta potential of the NPs were measured by dynamic light scattering method at room temperature, as well as in different pH solutions (pH = 5.5, 6.0, 6.5 and 7.0). Proteins on RBC@ICG NPs, RBC@ICG-DOX NPs and erythrocyte membranes were analyzed by sodium dodecyl sulfate-polyacrylamide gel electrophoresis (SDS-PAGE) at 100 V for 1.5 h, and stained with Coomassie blue for 4 h. The proteins were then analyzed in the erythrocyte membranes. RBC@ICG-DOX NPs were dissolved in DI water, PBS, FBS and DMEM, and the samples in different solvents were aspirated by capillary glass tubes at 0, 24 and 48 h, respectively. And the fluorescence intensities were observed under NIR-II fluorescence imaging system (SOPTOP NIR II-MS, China). During the preparation of the RBC@ICG-DOX NPs, the supernatant was collected from three centrifugation cycles. The absorption spectra of the supernatants collected after the washing step were determined using a UV spectrophotometer. The amount of ICG and DOX in the supernatant was determined from the corresponding calibration curves (absorbance intensity versus concentration) at 480 nm and 780 nm. The encapsulation rates of DOX and ICG were further calculated.

To determine the drug loading capacity (DLC) and encapsulation efficiency (EE), the supernatants of three centrifugation cycles were collected during the preparation of RBC@ICG-DOX NPs. The absorption spectra of the supernatant obtained following the washing step were determined using a UV spectrophotometer. The amount of ICG and DOX in the supernatant was determined based on the corresponding calibration curves (absorbance intensity versus concentration) at 480 nm and 780 nm. DLC and EE were calculated according to the following equations:

$$DLC(\%) = \frac{W_{DOX/ICG} - W_{Drug\ in\ supernatant}}{W_{RBC@ICG-DOX}} \times 100\%$$

$$EE(\%) = \frac{W_{DOX/ICG} - W_{Drug\ in\ supernatant}}{W_T} \times 100\%$$

In vitro Release of DOX

The drug release characteristics were determined in PBS by dialysis method.[14] PBS (pH=5.5) and PBS (pH=7.4) were used to simulate two different physiological environments. 1 mL of RBC@ICG-DOX NPs (DOX content of 20 μg mL^{-1}) was sealed into a dialysis bag (3500 Da, Spectrum USA) and placed in a beaker containing 50 mL of PBS (pH=5.5 or 7.4) and stirred at 37°C at 100 rpm. At specific time intervals (0.5, 1, 2, 4, 6, 8, 12, 24, 48 and 72 h), 3 mL of sample was collected for DOX release analysis and replaced with an equal volume of PBS. Owing to the photothermal effect of ICG in NPs, DOX release from RBC@ICG-DOX NPs was triggered by irradiation with 808 nm laser for 5 min before reaching the preset time point. The concentration of DOX released at different pH was analyzed by UV-visible NIR spectrophotometer at 480 nm to further calculate the cumulative DOX release.

In vitro Evaluation of PDT/PTT Performance

We selected the ABDA (reactive oxygen species detection reagent) for detecting the $^1O_2$ generated by the photosensitizer under 808 nm laser irradiation. ABDA solution (80 μL, 1 mg mL^{-1}, dissolved in DMSO) was then added into solutions of ICG and RBC@ICG-DOX NPs. The samples were then subjected to continuous laser irradiation (808 nm, 1 W cm^{-2}), and the absorption spectra of the mixtures were recorded every 5 minutes over a period of 40 minutes.

The photothermal properties of RBC@ICG-DOX NPs were investigated. The photothermal effects of PBS, DOX, ICG, and RBC@ICG-DOX NPs were analyzed under the irradiation of 808 nm laser at two power densities (0.5 and 1 W cm^{-2}), and then the temperature changes were recorded. In addition, the temperature changes of three different concentrations of RBC@ICG-DOX NPs solutions (equivalent to ICG concentrations of 5, 10, and 25 μg mL^{-1}) were analyzed under the irradiation of 808 nm laser (1 W cm^{-2}). Then, the RBC@ICG-DOX NPs (equivalent to ICG concentration, 10 μg mL^{-1}) were analyzed in three hot and cold cycles after irradiating them with an 808 nm laser (1 W cm^{-2}) to increase the temperature to a predetermined temperature and then naturally cooled to room temperature. The temperature change of each sample was recorded with a Fotric 323 Pro thermal camera at preset time intervals and the photothermal conversion efficiency was calculated. The following formula was used to calculate η:

$$\eta = \frac{M_D C_D \left(T_{max} - T_{surr,\,Water}\right)}{\tau_s I \left(1 - 10^{-A_{808}}\right)} \times 100\%$$

M_D and C_D are the mass and heat capacity of deionized water, Tmax and Tmax, water are the maximum equilibrium temperature of RBC@ICG-DOX NPs solution and water, τ_s is the system time constant, I is the NIR laser power, and A_{808} represents the absorbance at 808 nm.

Cells and Animals

Human cervical cancer cells (HeLa) and human cervical epithelial cells (H8) were obtained from the American Type Culture Collection (ATCC). HeLa cells and H8 cells were cultured in DMEM. Cells were cultured in a humid atmosphere (37°C, 5% CO_2) in a medium containing 10% fetal bovine serum and 1% penicillin–streptomycin.

BALB/c nude mice (female, 18–20 g) and BALB/c mice (female, 18–20 g) were purchased from Beijing Viton Lever Laboratories, and were housed in the Animal Experiment Center of Xinjiang Medical University. All animal procedures were approved by the Xinjiang Medical University Animal Experimentation Ethics Committee. All experimental operations were in compliance with the requirements under the management of the Animal Care and Use Committee of Xinjiang Medical University. All proposals were submitted and approved. All animal procedures were performed in accordance with the National Institutes of Health Guide for the Care and Use of Laboratory Animals and approved by the Animal Care and Use Committee of Xinjiang Medical University (IACUC-20200331-46).

Cytotoxicity Analysis

The cellular dark toxicity and phototoxicity of RBC@ICG-DOX NPs on HeLa cells were detected by CCK-8 assay. First, 5×10^3 cells/well were cultured in 96-well plates for 24 h until the cells were adherent to the wall. RBC@ICG-DOX NPs were dissolved in cell culture solution at different concentrations and incubated for 6–8 h, allowing the cells to take up RBC@ICG-DOX NPs. After co-incubation of RBC@ICG-DOX NPs with cells, 10 μL of CCK-8 assay solution was added to each well and incubated for 2–4 h under dark conditions, and then the optical density (OD) was recorded at 450 nm for cell viability assay of RBC@ICG-DOX NPs. Phototoxicity, on the other hand, was detected under laser (808 nm, 1 W cm^{-2}) irradiation for 5 min after 6–8 h of incubation. Cell viability was determined by comparing the OD values of the treated and control groups as follows:

$$cell\ viability(\%) = \frac{OD_{treatment} - OD_{blank}}{OD_{control} - OD_{blank}} \times 100\%$$

The $OD_{treatment}$, $OD_{control}$ and OD_{blank} were recorded for treatment, control and blank groups respectively. Each experiment was performed at least three times and cell viability was expressed as mean ± standard deviation.

https://doi.org/10.2147/IJN.S496982

Cellular Uptake

The cells were imaged using a laser confocal scanning microscope. 2×10^5 of HeLa cells were inoculated into cell culture dishes (35 mm diameter) with a glass bottom (0.13 mm thick) and cultured for 24 h. The HeLa cells were then co-incubated with complete media containing free ICG, free DOX and RBC@ICG-DOX NPs, respectively, for 2 h. After discarding the old media, the cells were rinsed three times with PBS. The cells were then stained with Hoechst 33342, fresh medium was added, and the cell images were obtained by confocal laser scanning microscopy with a 60 x objective lens.

Intracellular ROS Analysis

The reactive oxygen species assay was performed using the fluorescent probe DCFH-DA. A total of 2×10^5 HeLa cells were inoculated into a cell culture dish (35 mm in diameter) and incubated for 24 h. Subsequently, the HeLa cells were co-incubated in four groups (Control, Laser, RBC@ICG-DOX NPs and RBC@ICG-DOX NPs + Laser) of conditioned complete medium for 2 h. Prior to laser (808 nm, 1 W cm^{-2}, 5 min) irradiation, cells were incubated with the DCFH-DA probe for 30 min and then imaged with laser confocal microscopy.

Intracellular Photorelease of DOX

HeLa cells co-cultured with RBC@ICG-DOX NPs were observed by CLSM under continuous low power density (0.3 W cm^{-2}) laser irradiation at a wavelength of 808 nm to monitor the process of light-controlled DOX release. After 2×10^5 of HeLa cells were inoculated into two confocal dishes (35 mm diameter) and cultured for 24 h, RBC@ICG-DOX NPs were added and cultured for 1 h. The RBC@ICG-DOX NPs were then used to monitor the light-controlled DOX release process. The cells were then stained with the nuclear dye Hoechst 33342 for 10 min. Finally, the cells were placed in medium containing propidium iodide (PI) dye. One group of cells was then continuously irradiated with laser light and the other group served as a control, and cell fluorescence was monitored at 0, 0.5 and 1 h using the CLSM system.

In vitro PDT/PTT Synergistic Chemotherapy Evaluation

HeLa cells were inoculated into 4 cell culture dishes and cultured for 24 h. The cells were divided into several groups: Control, Laser irradiation (1 W cm^{-2}), RBC@ICG-DOX NPs and RBC@ICG-DOX NPs + Laser irradiation (1 W cm^{-2}). Then they were treated with Hoechst 33342 and PI staining. Finally, CLSM was performed on the four groups of cells and dead cells were labelled in red. Fluorescence images of HeLa cells were acquired using blue (DAPI) and red (PI) channels with excitation wavelengths of 405 nm and 545 nm, respectively.

This study used flow cytometry to assess the combined therapeutic effect of PTT, PDT and chemotherapy using RBC@ICG-DOX NPs on HeLa cells. The cells were then divided into four groups: the control group, the 808 nm laser group (1 W cm^{-2}, 5 min), the RBC@ICG-DOX NPs group and the RBC@ICG-DOX NPs with 808 nm laser group (1 W cm^{-2}, 5 min). Finally, the four groups of HeLa cells were washed with PBS, trypsin digested, and collected by centrifugation. The collected cells were washed twice more with PBS. The cell suspension was stained by sequentially adding PI probe and membrane-bound protein V-FITC.

In vivo Tumor-Retention Capacity of RBC@ICG-DOX NPs

The tumor-retention capacity of RBC@ICG-DOX NPs was evaluated by the in vivo fluorescence imaging technique. 100 μL of free ICG and RBC@ICG-DOX NPs (2 mg kg^{-1}) were injected into the tumors of nude mice, and the same amount of PBS was injected into the tumors of control nude mice, respectively. After 1 h of post-injection, the tumors were irradiated with an 808 nm laser with a power density of 1 W cm^{-2} for 5 min. After that, all nude mice were imaged by a small animal real-time imaging system (BLT, AniView) after 1, 5, 8, 24, 48 and 72 h.

In vivo Antitumor Evaluation

To evaluate the in vivo photothermal performance of RBC@ICG-DOX NPs, the nude mouse model of cervical cancer was established. The experimental group of nude mice received an intratumoral injection of RBC@ICG-DOX NPs (2 mg kg^{-1}) and were irradiated with an 808 nm (1 W cm^{-2}) laser. The control group received 50 μL of PBS injected into the tumor site

of cervical cancer tumour bearing nude mice. The temperature changes in the subcutaneous tumor sites of both groups were recorded using a Fotric 323 Pro thermal camera at preset time intervals and then compared.

To evaluate the synergistic effects of phototherapy and chemotherapy in vivo, nude mice with cervical tumors were randomly divided into four groups (4 mice per group): (1) Control with intratumoral injection of PBS (50 μL); (2) 808 nm laser (1 W cm^{-2}, 5 min) irradiation of the tumor site; (3) intratumoral injection of RBC@ICG-DOX NPs (2 mg kg^{-1}); (4) intratumoral injection of RBC@ICG-DOX NPs (2 mg kg^{-1}) + Laser (1 W cm^{-2}, 5 min) irradiation of the tumor site. Tumor volume and body weight were measured every two days after treatment and recorded continuously for 16 days. Afterwards, the tumors were excised and the mice were dissected.

Biosafety Evaluation

Toxicity of RBC@ICG-DOX NPs in major organs of mice was analyzed. RBC@ICG-DOX NPs (2 mg kg^{-1}) were injected into mice via tail vein and then mice were dissected after 24 h and 3 days. The major organs of mice such as heart, liver, spleen, lung and kidney were taken and stained for H&E. Finally, H&E sections were observed and analyzed with an inverted fluorescence microscope (Nikon TS2R-FL).

Statistical Analysis

All experiments were performed at least three times, and experimental data were expressed as mean ± standard deviation (SD). The two groups were compared using the unpaired two-tailed Student's *t*-test. Comparisons between multiple groups were performed using a one way or two-way ANOVA test. OriginLab software version 18.0 was used for statistical analysis. Differences are considered statistically significant with $*p < 0.05$, $**p < 0.01$, and $***p < 0.001$.

Results and Discussion

Preparation and Characterization of RBC@ICG-DOX NPs

Erythrocytes are an ideal source of cell membranes because they are easily isolated from the blood.[44] When NPs are modified with erythrocyte membranes, the presence of surface antigens enables these NPs to extend their circulation time in vivo by evading recognition and clearance by macrophages.[45] In this study, a biomimetic bilayer membrane nanocarrier system was constructed based on erythrocyte membranes, co-loaded with ICG and DOX, with the aim of combining PDT, PTT, and chemotherapy for more effective treatment of cervical cancer. The erythrocyte membrane can not only protect the NPs from premature release or leakage during blood circulation and improve their stability, but also be thermally disrupted during NIR laser irradiation, which triggers the accelerated release of the drug. Thus it could increase the drug concentration in the tumor area and ultimately improve the therapeutic efficacy with lower toxic side effects.

TEM images of RBC@ICG NPs and RBC@ICG-DOX NPs demonstrated the spherical morphology and uniform size of the NPs, which are bilayers encapsulated by liposomes and erythrocyte membranes as shown in Figure 1A and B. To verify the successful modification of RBC membranes, the types of membrane proteins were analyzed by SDS-PAGE. Figure 1C shows that the protein bands of erythrocyte membranes (I), RBC@ICG NPs (II) and RBC@ICG-DOX NPs (III) were well preserved without any significant difference. Zeta potential analysis shows that the surface charges of RBC@ICG and RBC@ICG-DOX NPs were −27.94 mV and −28.22 mV, respectively, which contributes to the great dispersion stability through electrostatic repulsion (Figure 1D). Furthermore, particle size stability experiments were conducted. As shown in Figure 1E, the average particle size of RBC@ICG-DOX NPs remained stable over 7 days, and the particle size of RBC@ICG-DOX NPs was also more stable under different pH environments (Figure 1F). The EE and DLC of RBC@ICG-DOX NPs were determined by absorption spectroscopy, respectively. The EE was calculated to be 93.2% and 75.7% for DOX and ICG, and the DLC was 6.3% and 2.0% for DOX and ICG, respectively. RBC@ICG-DOX NPs were dissolved in DI water, PBS, FBS, and DMEM, and no significant sedimentation was observed in the solution after 14 days, suggesting that the bilayer membrane-coated NPs have better stability (Figure S1). As shown in Figure 1G, free DOX and free ICG show characteristic absorption peaks at 480 nm and 780 nm, respectively, whereas the absorption peak at 780 nm seems to be slightly shifted for RBC@ICG-DOX NPs. This shift can be attributed to the interaction of ICG molecules with

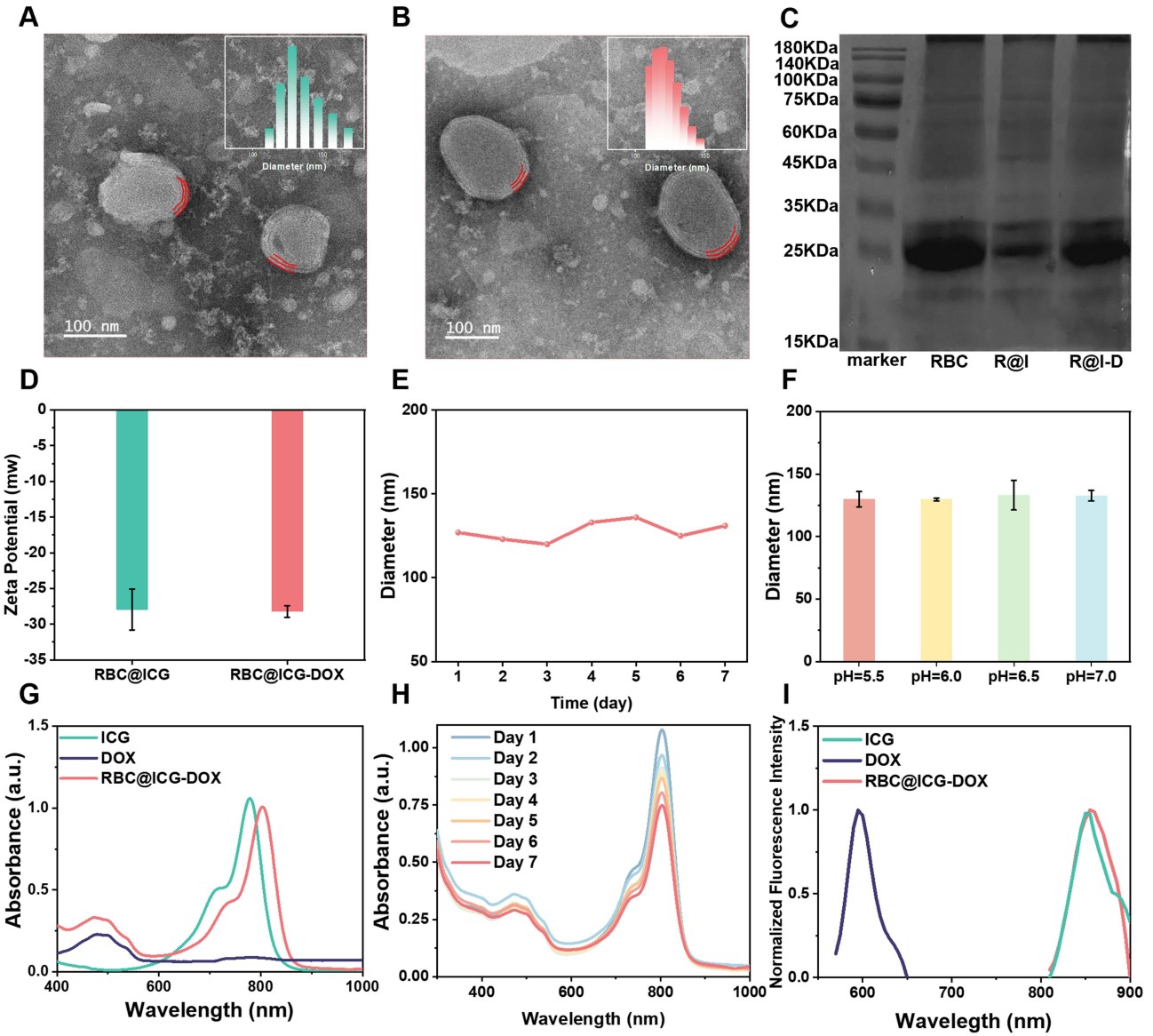

Figure 1 (**A**) TEM image of RBC@ICG NPs. Inset: DLS of RBC@ICG NPs. (**B**) TEM image of RBC@ICG-DOX NPs. Inset: DLS of RBC@ICG-DOX NPs. (**C**) Membrane protein analysis of RBC@ICG and RBC@ICG-DOX NPs. (I) erythrocyte membrane, (II) RBC@ICG, and (III) RBC@ICG-DOX NPs. (**D**) Surface zeta potential of RBC@ICG and RBC@ICG-DOX NPs. (**E**) Particle size stability of RBC@ICG-DOX NPs in aqueous solution for 1–7 days. (**F**) Particle size of RBC@ICG-DOX NPs in different pH values, n=3. (**G**) Absorption spectra of free ICG, free DOX and RBC@ICG-DOX NPs. (**H**) Absorption spectra of RBC@ICG-DOX NPs for seven consecutive days. (**I**) Fluorescence spectra of free ICG, free DOX and RBC@ICG-DOX NPs.

phospholipids and membrane proteins, leading to alterations in the molecular energy levels of ICG.[46,47] The absorption peaks of the RBC@ICG-DOX NPs appeared at 480 nm and 803 nm, which again suggests that the erythrocyte membrane was successfully modified on the surface of the NPs. A slight decrease in the absorption peak of the aqueous solution of RBC@ICG-DOX NPs was observed for 7 consecutive days (Figure 1H). The fluorescence spectra of free ICG, free DOX and RBC@ICG-DOX NPs were determined. As shown in Figure 1I, the fluorescence peak of free ICG was located at 850 nm, the fluorescence peak of free DOX was located at 600 nm, and the fluorescence peak of RBC@ICG-DOX NPs was located at 854 nm.

The fluorescence stability of RBC@ICG-DOX NPs in different solutions (DI water, PBS, FBS, DMEM) was analyzed at 0, 24 and 48 h (Figure S2) using NIR-II fluorescence microscopic imaging and quantified (Figure 2A). The fluorescence intensity of RBC@ICG-DOX NPs was notably higher in the FBS solution compared to other solutions, with a decrease in fluorescence intensity over time of less than 5%. Furthermore, the fluorescence stability of RBC@ICG-DOX NPs in various acidic solutions

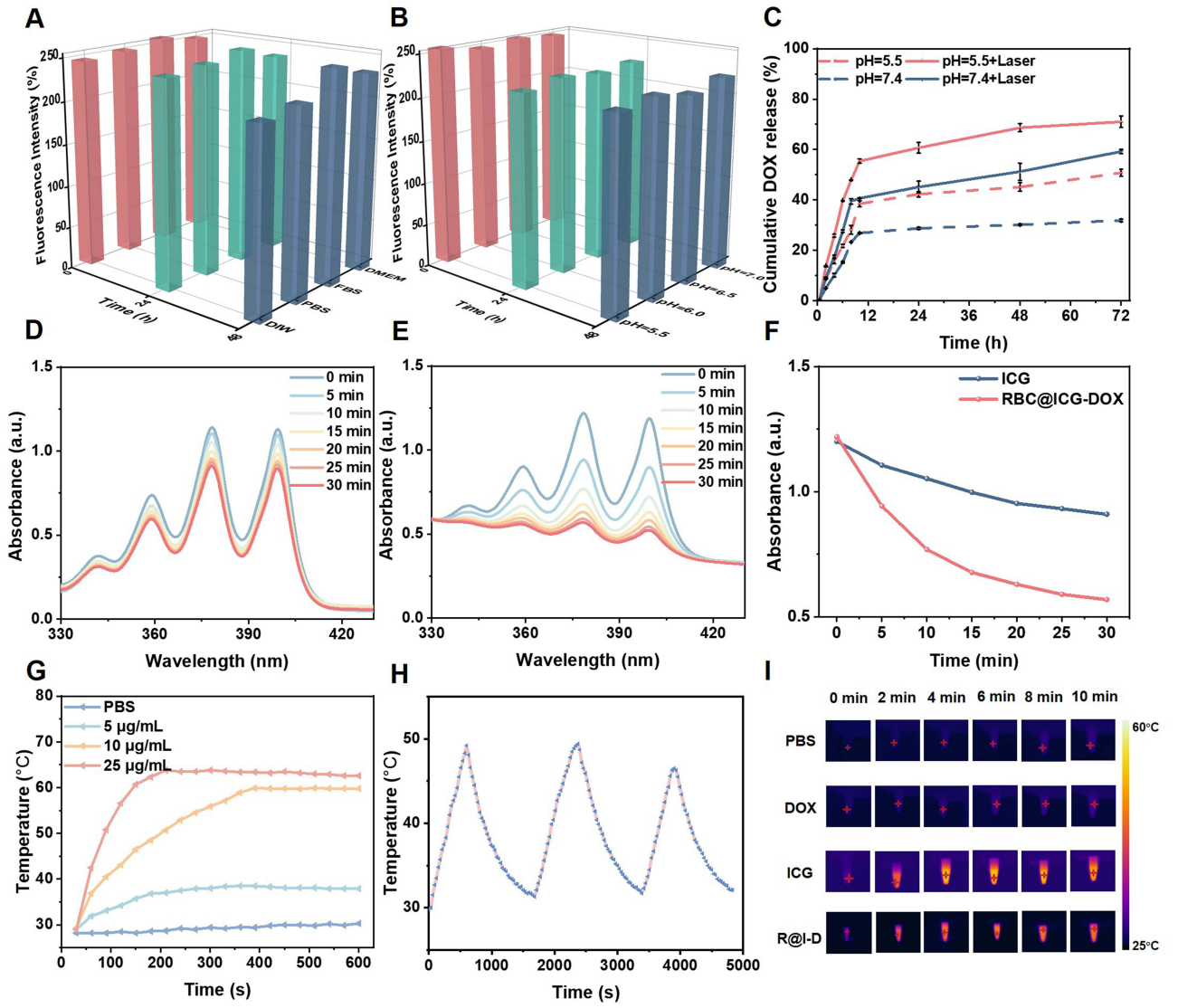

Figure 2 (**A**) Fluorescence intensity analysis of RBC@ICG-DOX NPs in different solutions. (**B**) Fluorescence intensity analysis of RBC@ICG-DOX NPs in different pH environments. (**C**) DOX release profiles of RBC@ICG-DOX NPs with and without laser irradiation under different pH conditions (n=3). (**D**) ICG produced $^1O_2$. (**E**) RBC@ICG-DOX NPs produced $^1O_2$. (**F**) Decay curves of ICG and RBC@ICG-DOX NPs absorption at 375 nm after irradiation for different times. (The power density of the 808 nm laser was 1 W cm^{-2} in all experiments). (**G**) Temperature rise versus time curves for different concentrations of RBC@ICG-DOX NPs. (**H**) Photothermal stability of RBC@ICG-DOX NPs during three heating-cooling cycles (ICG concentration of 10 μg mL^{-1}). (**I**) Infrared thermal images of different sample groups after 10 min irradiation with 808 nm laser (1 W cm^{-2}) for PBS, DOX, ICG, and RBC@ICG-DOX NPs.

(pH = 5.5, 6, 6.5 and 7.0) at 0, 24, and 48 h (Figure S3) was observed and quantitatively analyzed (Figure 2B). The results revealed that the fluorescence intensity of RBC@ICG-DOX NPs remained stable, with a decrease of less than 15% observed in all cases. These findings indicate that RBC@ICG-DOX NPs are well-suited for in vivo environmental and fluorescence imaging applications.

In vitro Release of DOX

The release of DOX from laser-irradiated RBC@ICG-DOX NPs in PBS solutions were evaluated at pH=7.4 and pH=5.5, as shown in Figure 2C. Laser irradiation significantly accelerated DOX release from RBC@ICG-DOX NPs in both pH=7.4 and pH=5.5 PBS solutions. Regardless of laser irradiation, DOX release from RBC@ICG-DOX NPs at pH=5.5 was slightly faster than at pH=7.4, due to the faster dissolution of DOX in an acidic medium. In the laser-irradiated group, RBC@ICG-DOX NPs at pH=5.5 released more than 70% of DOX after 10 h. Similar results were observed at

https://doi.org/10.2147/IJN.S496982

pH=7.4, suggesting that the elevated temperature of the carrier system contributes to the disintegration of RBC@ICG-DOX NPs, thereby promoting DOX release. Given the weakly acidic microenvironment of tumor tissues, this laser-triggered nanoparticle release in an acidic environment accelerates drug release within tumor cells, enhancing the therapeutic effect.

In vitro Evaluation of PDT/PTT Performance

The extent of $^1O_2$ production after 808 nm laser irradiation was assessed using the ABDA probe.[48] To verify $^1O_2$ production, ABDA was added to free ICG and RBC@ICG-DOX NPs, respectively, and the absorption at 375 nm was monitored. Figure 2D and E show that the absorption of both free ICG and RBC@ICG-DOX NPs groups decreased with the increase of irradiation time. The absorption of free ICG decreased by 9.2% compared to its original value, while the absorption of RBC@ICG-DOX NPs exhibited a significantly greater reduction of 44.2% (Figure 2F). This pronounced decrease can be attributed to the fact that the absorption peaks of RBC@ICG-DOX NPs were more red-shifted than those of free ICG, making them more suitable for 808 nm excitation laser. These experiments demonstrated that RBC@ICG-DOX NPs could effectively generate $^1O_2$ under irradiation of 808 nm laser.

In order to investigate the photothermal properties of RBC@ICG-DOX NPs, the temperature changes of the test solutions were recorded under 808 nm laser irradiation. Figure S4 shows the photothermal temperature profiles of PBS, ICG, and RBC@ICG-DOX NPs (equivalent to ICG concentration of 8 μg mL^{-1}) under 808 nm laser (0.5 W cm^{-2}) irradiation. The warming effect of RBC@ICG-DOX NPs was more significant when the laser power density was increased to 1 W cm^{-2} (Figure S5). In this study, the ICG converts NIR light energy into thermal energy, which including a part of PTT and the other part for controlling DOX release. In addition, ICG is also a multifunctional molecule that is used in PDT and NIR imaging. Although the photothermal efficiency of RBC@ICG-DOX NPs is lower than free ICG, the photodynamic effect is enhanced at a fixed excitation light. The temperature of the RBC@ICG-DOX NPs could be increased from 29.5°C to 56.1°C within 10 min. In addition, the temperature increased significantly as the concentration of RBC@ICG-DOX NPs increased (Figure 2G). The results indicated that the temperature produced by laser irradiation of RBC@ICG-DOX NPs was proportional to the concentration and power density. The photothermal stability of RBC@ICG-DOX NPs was evaluated by the cold/heat cycling experiment, in which RBC@ICG-DOX NPs underwent three heating/cooling cycling processes of laser irradiation (Figure 2H). Figure S6 observed that the photothermal conversion efficiency of RBC@ICG-DOX NPs reached 20.8%. Infrared thermal images obtained through infrared thermography clearly demonstrated that the temperatures of PBS and free DOX exhibited minimal variation. In contrast, the temperatures of free ICG, and RBC@ICG-DOX NPs showed a significant increase (Figure 2I).

Cytotoxicity Analysis

The biosafety of RBC@ICG-DOX NPs was evaluated using the CCK-8 assay. As shown in Figure S7, the viability of HeLa cells was 71.48% even when the concentration of ICG in RBC@ICG-DOX NPs reached 16 μg mL^{-1}, indicating that RBC@ICG-DOX NPs have low cytotoxicity and good biocompatibility. In addition, cytotoxicity experiments were performed by H8 cells. The final results showed that the cell survival rate was 85%, respectively, indicating that the RBC@ICG-DOX NPs had low cytotoxicity and good biocompatibility (Figure S8). The study evaluated the phototoxicity of RBC@ICG-DOX NPs on HeLa cells. The results showed that when the concentration of ICG in RBC@ICG-DOX NPs was 16 μg mL^{-1}, irradiated with 808 nm laser (1 W cm^{-2}), ICG produced PDT/PTT effect and DOX produced chemotherapeutic effect. This reduced the viability of HeLa cells to 20.71%. The results showed that RBC@ICG-DOX NPs had good phototoxicity under laser irradiation, produced a lot of heat and ROS, and led to the death of tumor cells.

Cellular Uptake

Cellular uptake is a crucial factor in drug delivery. In this study, we investigated the uptake of RBC@ICG-DOX NPs by HeLa cells using confocal laser scanning microscopic imaging. HeLa cells were incubated with free ICG, free DOX, and RBC@ICG-DOX NPs for 2 h, respectively. The nuclei were then stained with DAPI (blue) and confocal fluorescence images of the cells were obtained using CLSM as shown in Figure 3A. In addition, we observed intracellular ROS production using confocal microscopy (Figure 3B). In Figure 3A, we observed the

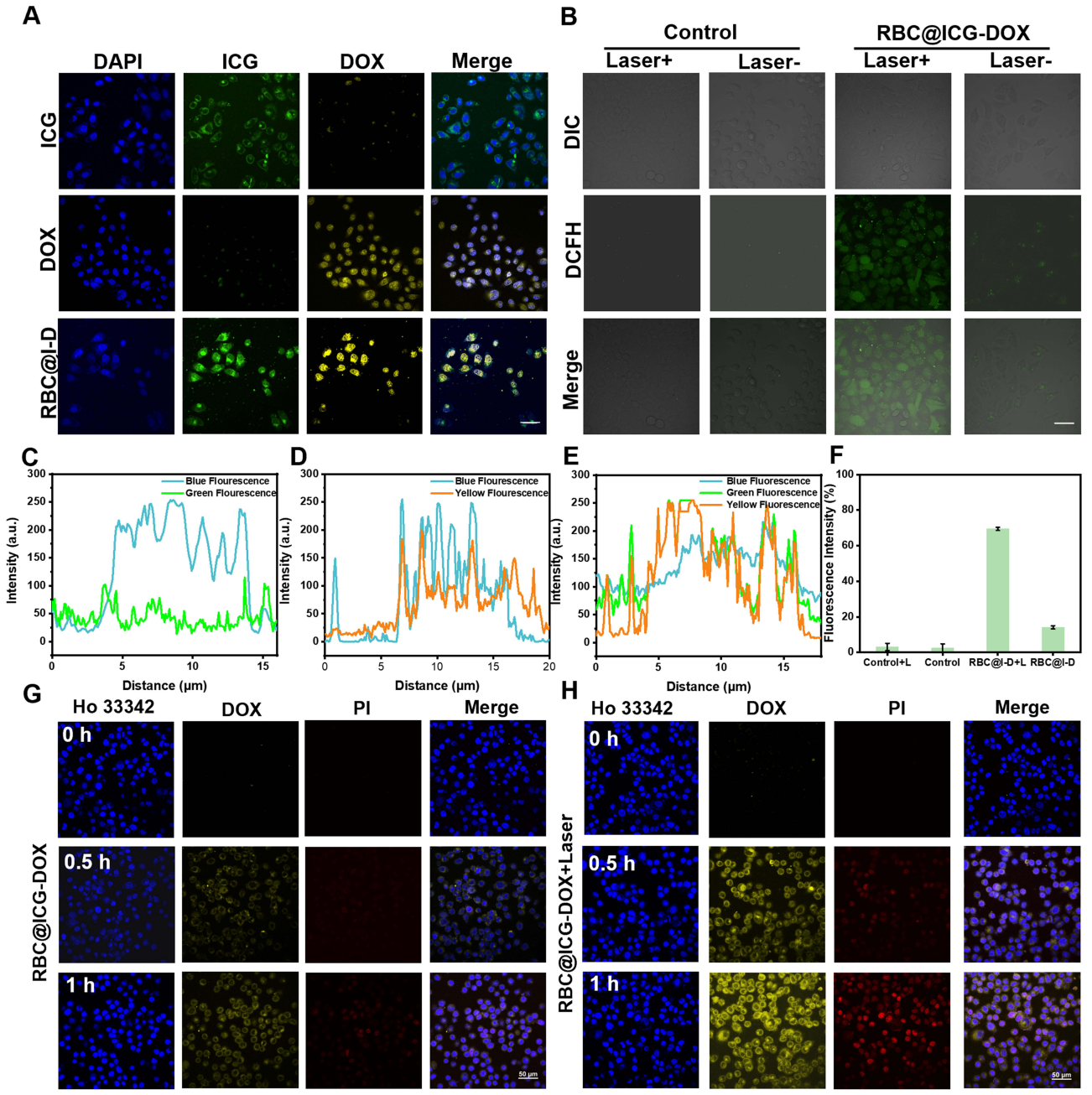

Figure 3 (**A**) Cellular uptake analysis of free ICG, free DOX and RBC@ICG-DOX NPs after co-incubation treatment with HeLa cells in cell confocal images. (**B**) CLSM fluorescence images (scale bar: 50 μm) of DCFH-DA-stained HeLa cells treated with Control, Laser, RBC@ICG-DOX NPs, and RBC@ICG-DOX NPs + Laser. Fluorescence intensity profiles of (**C**) ICG, (**D**) DOX and (**E**) RBC@ICG-DOX NPs. (**F**) The fluorescence intensity analysis of intracellular ROS. (**G**) CLSM image of RBC@ICG-DOX NPs co-incubated with HeLa cells. (**H**) CLSM image of RBC@ICG-DOX NPs co-incubated with HeLa cells under 808 nm laser irradiation.

uptake of RBC@ICG-DOX NPs by HeLa cells using confocal microscopy. After different treatments, the yellow fluorescence of DOX was mostly located in the nucleus, and the green fluorescence of ICG was dispersed in the cytoplasm. In contrast, the free ICG and free DOX cultured HeLa cells exhibited fluorescence in the green and yellow channels, respectively (Figure 3C–E). The results showed that RBC@ICG-DOX NPs were well taken up by HeLa cells and could label HeLa cells more efficiently.

https://doi.org/10.2147/IJN.S496982

Intracellular ROS Analysis

To assess the efficiency of ROS generation in tumor cells treated with RBC@ICG-DOX NPs, DCFH-DA was employed as a probe to measure intracellular ROS levels. The DCFH-DA probe can pass through the cell membrane without significant autofluorescence.[49] When degraded by intracellular lipases to DCF and oxidized by ROS, it emits fluorescence (in green channel). This property enables the assessment of cellular ROS generation. Figure 3B shows that the group of HeLa cells, to which only the DCHF-DA probe was administered, exhibited almost no significant fluorescence signals in the absence of laser irradiation. Furthermore, the same fluorescence (in green channel) was not produced after laser irradiation. In the experimental group, HeLa cells were co-incubated with RBC@ICG-DOX NPs for 2 h. The fluorescence intensity of the laser-irradiated group was 4.9 times higher than that of the non-laser-irradiated group (Figure 3F). Cell dysfunction and apoptosis can occur when the balance of the complete redox system in cells is disrupted. The study found that laser irradiation caused RBC@ICG-DOX NPs to generate a significant amount of ROS within cells, resulting in the death of HeLa cells.

Intracellular Photorelease of DOX

Studies have shown that DOX enters the cell membrane firstly and then the nucleus.[50] As shown by the fluorescence in Figure 3G, DOX was dispersed in the cytoplasm after entering the cell, and a few nuclei turned bright fluorescence after 1 h, indicating that DOX had successfully entered the nucleolus. DOX, as a typical anticancer chemotherapeutic drug, can inhibit DNA and RNA replication and transcription through inhibition of topoisomerase I as well as insertion into the DNA and RNA strands.[51,52] Figure 3H illustrates the drug release and cell viability under low power density irradiation with an 808 nm laser. The results show that more DOX was released from the carrier and penetrated into the nucleolus after 1 h compared to the non-laser irradiated group. This led to a significant increase in apoptosis among HeLa cells, attributed to the PTT effect triggered by the low-power-density laser, which accelerates DOX release and thereby enables faster tumor treatment. These experiments demonstrate that RBC@ICG-DOX NPs are an effective carrier for laser-triggered drug release and confirm that DOX exerts a chemotherapeutic effect on cells upon release.

In vitro PDT/PTT Synergistic Chemotherapy Evaluation

To further validate the synergistic anti-tumor efficacy of PTT, PDT, and chemotherapy using the synthesized RBC@ICG-DOX NPs, we assessed the anti-tumor effect through live-dead cell Hoechst/PI double staining reagent (Figure 4A–D). Cell death was observed using continuous laser confocal microscopy. The control and laser groups exhibited fewer PI fluorescence signals, indicating a relatively low inhibitory effect on HeLa cells. Following treatment with RBC@ICG-DOX NPs, the red fluorescence signal was approximately 45%. In HeLa cells treated with RBC@ICG-DOX NPs in conjunction with laser exposure, a significantly enhanced fluorescent signal (85%) in red channel was detected (Figure 4E). These results indicated that the combination chemotherapy of PDT and PTT with RBC@ICG-DOX NPs had better ablation effects on cervical cancer cells. The stark contrast observed between the RBC@ICG-DOX NPs group and the RBC@ICG-DOX NPs + Laser group further substantiates the therapeutic mechanism of our nanosystems. The localized thermal effect of PTT under NIR light irradiation can enhance blood flow rates, thereby increasing oxygen supply and improving the therapeutic efficacy of PDT. This interaction may lead to a synergistic effect between PTT and PDT, as PTT facilitates the release of DOX, resulting in a combined therapeutic approach that significantly enhances treatment outcomes. Furthermore, the antitumor properties of RBC@ICG-DOX NPs were verified by flow cytometry. Figure 4F shows that apoptosis was minimal in the Q2 and Q3 quadrants of cells treated with only 808 nm laser irradiation and only RBC@ICG-DOX NPs, at approximately 5.49% and 9.64%. However, the Q2 and Q3 quadrants of cells treated with RBC@ICG-DOX NPs + Laser irradiation exhibited a higher level of apoptosis, at approximately 15.39%. The study confirmed that RBC@ICG-DOX NPs exhibit enhanced biological safety and robust therapeutic efficacy when subjected to 808 nm laser irradiation.

In vivo Tumor-Retention Capacity of RBC@ICG-DOX NPs

Rapid clearance of chemotherapeutic agents from tumors is one of the major causes of cancer chemotherapy failure. To avoid this, the drug is encapsulated by a biomimetic bilayer membrane nanocarrier, which effectively prevents the drug from being rapidly washed away by the bloodstream to prolong its retention time in the tumor[38] and improve the safety

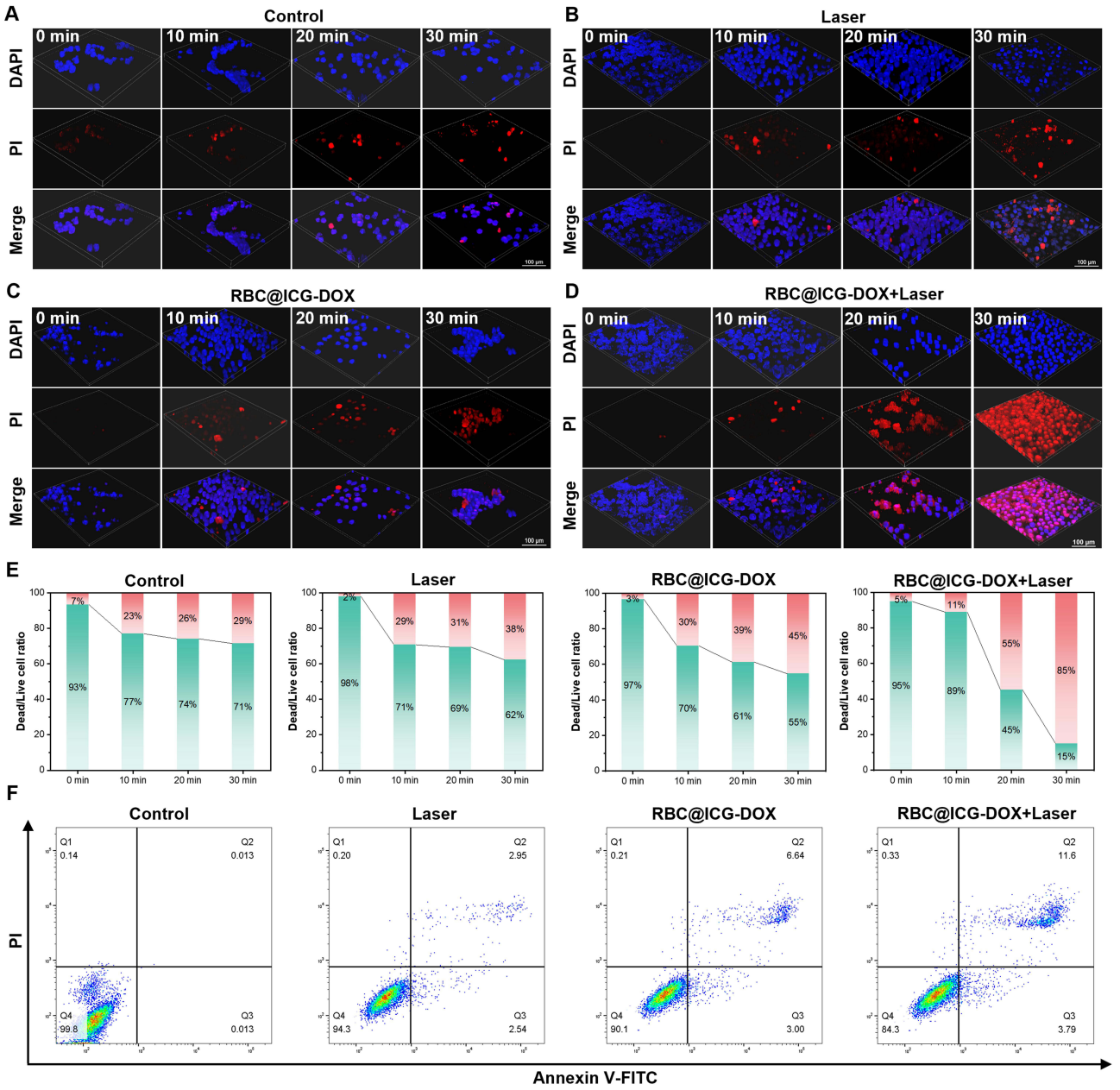

Figure 4 Confocal laser scanning microscopy (CLSM) images of (**A**) Control, (**B**) Laser, (**C**) RBC@ICG-DOX NPs and (**D**) RBC@ICG-DOX NPs + Laser treated HeLa cells (scale bar: 100 μm). (**E**) Quantitative analysis of (**A**–**D**). (**F**) Flow cytometry analysis of membrane-bound protein V-FITC and PI staining.

of the nanomedicine. Figure 5A displays the fluorescence imaging of nude mice following the injection of PBS, free ICG and RBC@ICG-DOX NPs. In Figure 5B, the fluorescence decay curves of the tumors are shown at different times. It is clear that the fluorescence intensity of tumor sites in nude mice treated with RBC@ICG-DOX NPs was significantly stronger than that observed in tumors treated with free ICG after 72 h. This erythrocyte membrane modification allows the NPs to bypass clearance by the immune system and extends their circulation time in the body. Figure 5C presents a schematic diagram of the tumor section treated with RBC@ICG-DOX NPs, and Figure 5D displays two tumor tissue sections observed under the NIR-II fluorescence microscopic imaging system at different magnifications (1 ×, 3 ×, 5 ×). Fluorescence signals were concentrated at the edges of the tumor sections, and the fluorescence inside the tumors was weak. The results, calculated based on the distribution of fluorescence intensities, are shown in Figure 5E. These findings suggest that RBC@ICG-DOX NPs entered the tumor and aggregated on the tumor surface.

https://doi.org/10.2147/IJN.S496982

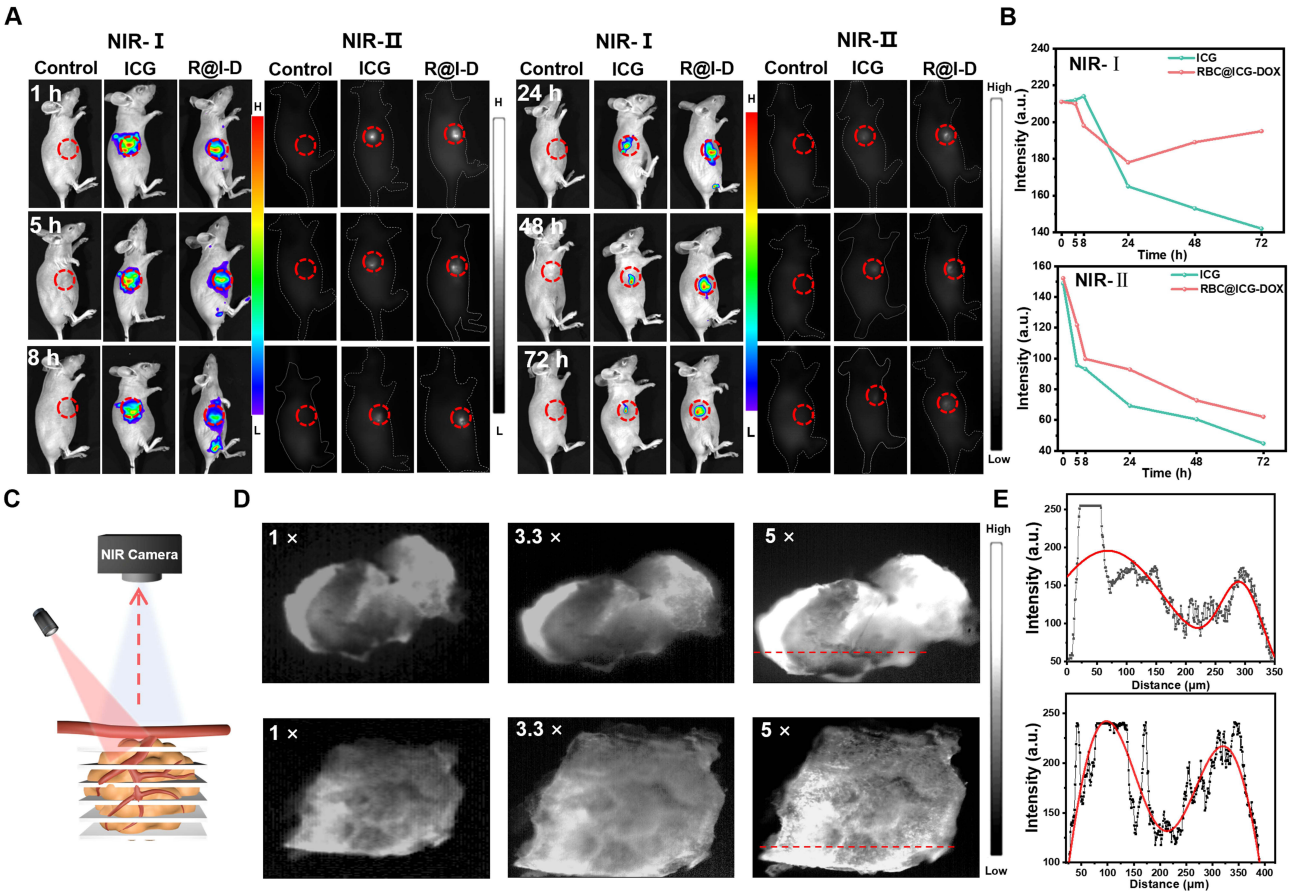

Figure 5 (**A**) Retention ability of RBC@ICG-DOX NPs in tumor-bearing mice. In vivo NIR-I and NIR-II fluorescence imaging photographs of mice at different times after drug administration. Mouse tumors were injected with PBS (control), free ICG and RBC@ICG-DOX NPs. (**B**) The fluorescence decays in tumors after various treatments. (**C**) Schematic of tumor sections. (**D**) NIR-II fluorescence imaging of tumor sections at different magnifications. (**E**) Spatial resolution analysis (black line) and Gaussian fitting of the red line.

In vivo Antitumor Evaluation

Figure 6A shows the experimental flow chart for the in vivo antitumor investigation. To evaluate the in vivo photothermal efficacy of RBC@ICG-DOX NPs, tumor bearing nude mouse were selected for the experiment. The experimental group was injected with 100 μL of RBC@ICG-DOX NPs intratumorally at the tumor site, and the control group was injected with 100 μL of PBS and irradiated with an 808 nm laser (1 W cm^{-2}). Figure 6B illustrates a schematic diagram of the in vivo photothermal effect. Infrared thermography was used to record the warming (Figure 6C), and the temperature of the tumor region treated with PBS rose to a maximum of 36.6°C after 10 minutes. In contrast, the temperature of the tumor site treated with RBC@ICG-DOX NPs rose to 47.9°C (Figure 6D). These results indicate that the RBC@ICG-DOX NPs are an effective photothermal agent for PTT by releasing thermal energy at the tumor site under laser irradiation.

Further in vivo antitumor studies were performed on RBC@ICG-DOX NPs and BALB/c nude mice bearing HeLa tumors were used as animal models. Nude mice were treated with different conditions of PBS, PBS+Laser, RBC@ICG-DOX NPs and RBC@ICG-DOX NPs + Laser. Tumor growth was monitored for up to 16 days to assess the synergistic treatment effect of photothermal, photodynamic and chemotherapy. The results showed that tumor growth was inhibited in the drug-treated group during the 16-day observation period, and Figure 6E is an image of the excised tumor on day 16. Figure 6F and G are the changes in body weight of the mice and the relative volume of the tumors in vivo during the 16-day period. Figure 6H is the tumor weight of the mice. It was worth noting that the RBC@ICG-DOX NPs + Laser group achieved 88.7% tumor growth inhibition (Figure 6I). Images of nude mice after treatment with different treatment groups (Figure 6J). In contrast, the tumor size of PBS and laser-treated tumors showed a continuous growth trend, suggesting that PBS or laser irradiation alone could not inhibit tumor growth. The relative reduction in tumor size of

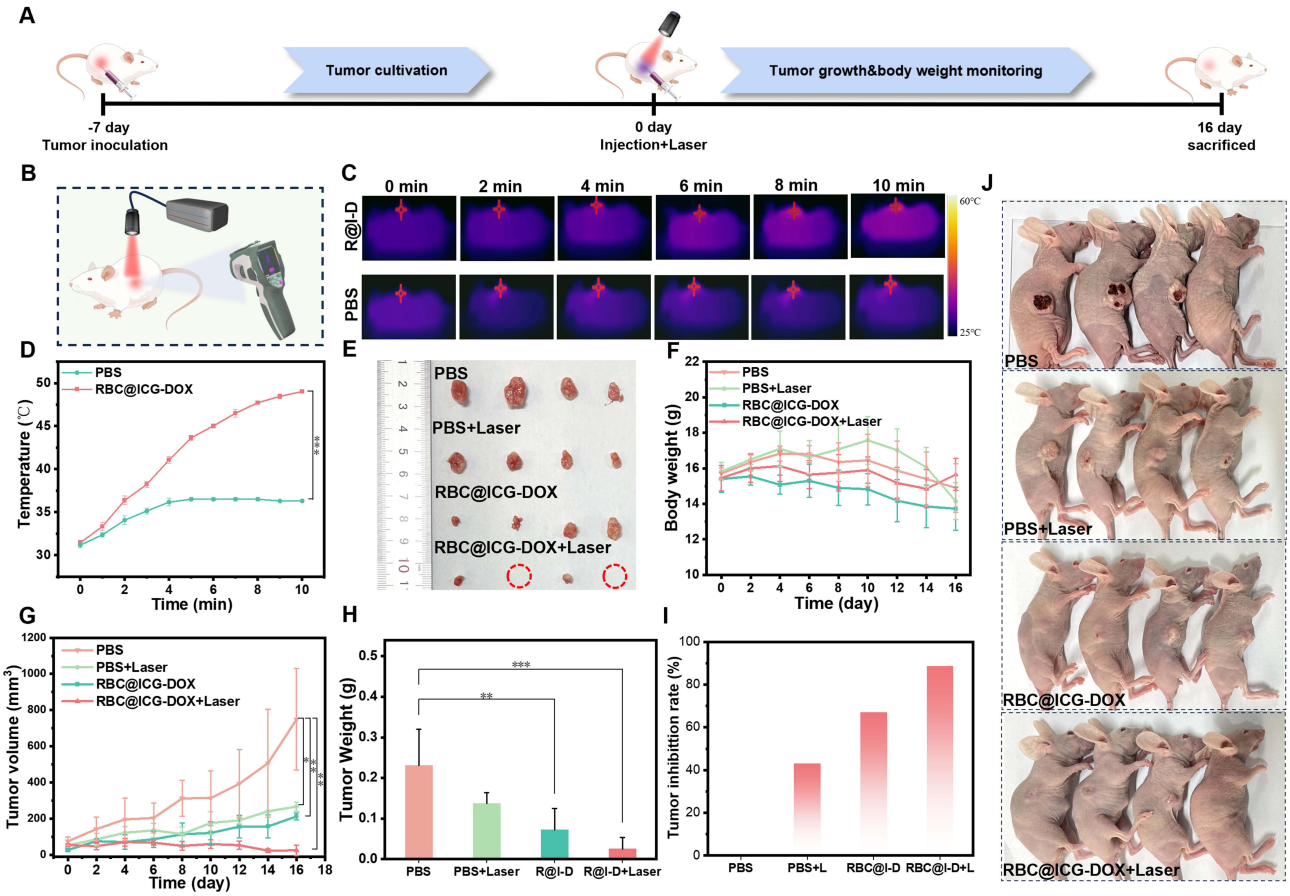

Figure 6 In vivo antitumor efficiency assessment. (**A**) Experimental flowchart of in vivo antitumor study. (**B**) Schematic diagram of mice irradiated with NIR laser. (**C**) Infrared thermogram of a mouse irradiated with a NIR laser for 10 min. (**D**) Temperature changes at the tumor site during laser irradiation in the control (PBS injection) and RBC@ICG-DOX NPs groups (n=3). (**E**) Tumor pictures of mice in different intervention groups after 16 days of treatment (n=4). (**F**) Body weight changes of mice in different intervention groups during the treatment period. (**G**) Tumor volume changes of mice in different intervention treatment groups during the treatment period. (**H**) Tumor weight of mice. (**I**) Tumor growth inhibition after different interventional treatments. (**J**) Pictures of mice after 16 days of treatment with different interventions. *p<0.05,**p<0.01,***p<0.001.

tumors treated with RBC@ICG-DOX NPs suggests that the chemotherapeutic agent DOX exerted some tumor inhibitory effect in the absence of laser intervention. Finally, RBC@ICG-DOX NPs with laser tumors disappeared or were reduced in size, and these data suggest that RBC@ICG-DOX NPs have excellent photothermal, photodynamic and chemotherapeutic effects.

Biosafety Evaluation

To investigate whether RBC@ICG-DOX NPs would threaten healthy tissues and organs, fresh blood from mice was collected for routine blood and biochemical blood tests (Figure 7A). All blood parameters from mice administered with RBC@ICG-DOX NPs were within the normal range of healthy mice. The in vivo toxicity of the RBC@ICG-DOX NPs was further evaluated by histological studies in mice. As shown in Figure 7B, microscopic images of H&E-stained tissues showed that no significant short-term (24 h post-injection) and long-term (3 days post-injection) damage or inflammatory lesions were observed in all major organs (heart, liver, spleen, lung, and kidney) of the mice. Our results suggest that RBC@ICG-DOX NPs have a favorable biosafety profile.

https://doi.org/10.2147/IJN.S496982

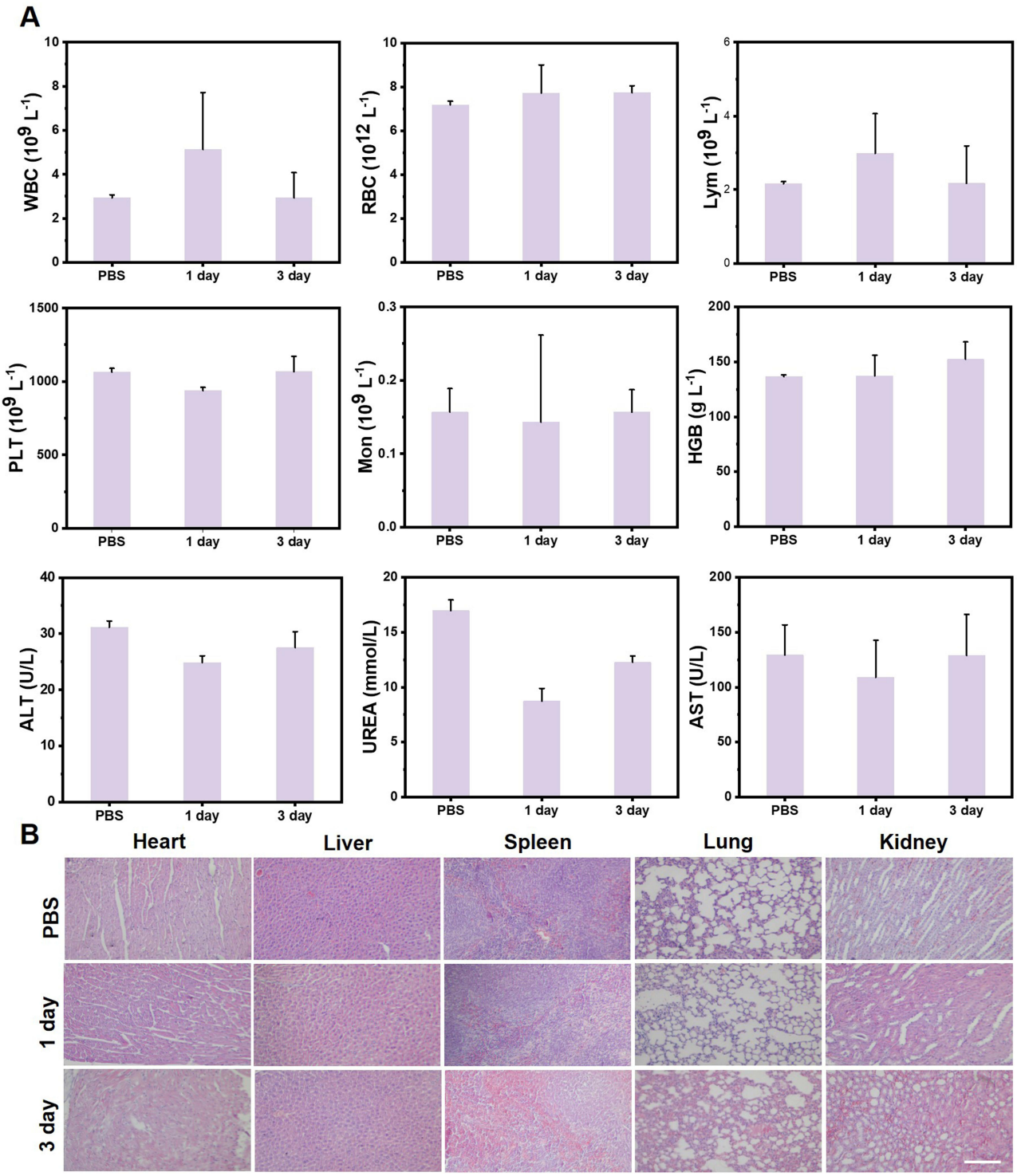

Figure 7 (**A**) Haematological indices of mice after 1 and 3 days of intravenous injection of RBC@ICG-DOX NPs (n=3). (**B**) Histological analysis of major organs (heart, liver, spleen, lung and kidney) in mice 1 and 3 days after intravenous injection of RBC@ICG-DOX NPs (scale bar: 100 μm).

Conclusion

In this study, a bilayer bionic membrane modification strategy was proposed to load ICG and the chemotherapeutic drug DOX, which have good photodynamic and photothermal effects, into a bilayer membrane nanocarrier. The nanosystem effectively reduced drug leakage and prolonged the circulation time of the drugs in the body. Both in vitro and in vivo

experiments showed that RBC@ICG-DOX NPs had higher biosafety and better therapeutic efficacy, suggesting that the combination of PDT, PTT and chemotherapy could significantly inhibit tumor growth. Our study achieved drug delivery, imaging and tumor synergistic therapy through combinatorial strategies as well as bilayer membrane encapsulation, opening up a new platform for the design of future tumor combination therapies. However, based on the properties of erythrocyte membranes, our materials only relied on passive targeting, and subsequent novel synergistic therapeutic platforms should focus more on active targeting of materials.

Abbreviations

PDT, photodynamic therapy; PTT, photothermal therapy; ICG, Indocyanine green; TEM, transmission electron microscopy; $^1O_2$, singlet oxygen; SDS-PAGE, sodium dodecyl sulfate-polyacrylamide gel electrophoresis; ROS, reactive oxygen species; RBC@I-D, RBC@ICG-DOX; RBC@I, RBC@ICG; DLS, dynamic light scattering.

Acknowledgments

This work was supported by the Xinjiang Uygur Autonomous Region Natural Science Foundation Youth Top Talent Project (No. 2022TSYCCX0032), Xinjiang Uygur Autonomous Region Regional Collaborative Innovation Special Science and Technology Assistance Program (No. 2022E02130), Xinjiang Uygur Autonomous Region Natural Science Foundation (No. 2022D01D40), the National Natural Science Foundation of China (NSFC) under Grant (Program No. 52250007, No. 82073475, No. 62035011, No. 82202220 and No. 82060326), Xinjiang Uygur Autonomous Region Natural Science Foundation Outstanding Youth Project (No. 2023D01E06), State Key Laboratory of Pathogenesis, Prevention and treatment of High Incident Diseases in central Asia (Nos. SKL-HIDCA-2022-3 and SKL-HIDCA-2022-GJ1). Xinjiang Uygur Autonomous Region University Research Program Project (XJEDU2022P058), Research and Innovation Team Project of Xinjiang Medical University:XYD2024C03. This work was supported by the Project of Tianchi Talent Distinguished Professor program in Xinjiang Uygur Autonomous Region (NO. 03010511).

Disclosure

The authors report no conflicts of interest in this work.

References

1. Cai Y, Si W, Huang W, et al. Organic dye based nanoparticles for cancer phototheranostics. *Small*. 2018;14(25):1704247.
2. Feng G, Liu B. Aggregation-Induced Emission (AIE) dots: emerging theranostic nanolights. *Acc Chem Res*. 2018;51:1404–1414. doi:10.1021/acs.accounts.8b00060
3. Lv R, Raab M, Wang Y, et al. Nanochemistry advancing photon conversion in rare-earth nanostructures for theranostics. *Coord Chem Rev*. 2022;460:214486.
4. Lv R, Wang Y, Lin B, et al. Targeted luminescent probes for precise upconversion/NIR II luminescence diagnosis of lung adenocarcinoma. *Anal Chem*. 2021;93(11):4984–4992. doi:10.1021/acs.analchem.1c00374
5. Tang Y, Wang G. NIR light-responsive nanocarriers for controlled release. *J Photochem Photobiol C*. 2021;47(1):100420. doi:10.1016/j.jphotochemrev.2021.100420
6. Zhou Z, Wang X, Zhang H, et al. Activating layered metal oxide nanomaterials via structural engineering as biodegradable nanoagents for photothermal cancer therapy. *Small*. 2021;17(12):2007486. doi:10.1002/smll.202007486
7. Zhou Z, Li B, Shen C, et al. Metallic 1T phase enabling MoS2 nanodots as an efficient agent for photoacoustic imaging guided photothermal therapy in the Near-infrared-II window. *Small*. 2020;16(43):2004173. doi:10.1002/smll.202004173
8. Luo S, Tan X, Fang S, et al. Mitochondria-targeted small-molecule fluorophores for dual modal cancer phototherapy. *Adv Funct Mater*. 2016;26(17):2826–2835.
9. Luo GF, Chen WH, Lei Q, et al. A triple-collaborative strategy for high-performance tumor therapy by multifunctional mesoporous silica-coated gold nanorods. *Adv Funct Mater*. 2016;26(24):4339–4350. doi:10.1002/adfm.201505175
10. Ge R, Cao J, Chi J, et al. NIR-guided dendritic nanoplatform for improving antitumor efficacy by combining chemo-phototherapy. *Int J Nanomed*. 2019;14:4931–4947. doi:10.2147/IJN.S203171
11. Deng Y, Guo M, Zhou L, et al. Prospects, advances and biological applications of MOF-based platform for the treatment of lung cancer. *Biomater Sci*. 2024;12(15):3725–3744. doi:10.1039/D4BM00488D
12. Liu J, Wang R, Zhai F, et al. A nanozyme composite with high near-infrared photothermal ability for synergistic bacterial elimination. *Mater Chem Front*. 2023;7(8):1642–1649. doi:10.1039/D2QM01239A
13. Gao J, Wang F, Wang S, et al. Hyperthermia-triggered on-demand biomimetic nanocarriers for synergetic photothermal and chemotherapy. *Adv Sci*. 2020;7(11):1903642. doi:10.1002/advs.201903642
14. Su J, Sun H, Meng Q, et al. Bioinspired nanoparticles with NIR-controlled drug release for synergetic chemophotothermal therapy of metastatic breast cancer. *Adv Funct Mater*. 2016;26(41):7495–7506. doi:10.1002/adfm.201603381

15. Xie Z, Fan T, An J, et al. Emerging combination strategies with phototherapy in cancer nanomedicine. *Chem Soc Rev*. 2020;49(22):8065–8087. doi:10.1039/D0CS00215A
16. Chen Z, Wang W, Li Y, et al. Folic acid-modified erythrocyte membrane loading dual drug for targeted and chemo-photothermal synergistic cancer therapy. *Mol Pharm*. 2020;18(1):386–402. doi:10.1021/acs.molpharmaceut.0c01008
17. Chen J, Li X, Zhao X, et al. Doxorubicin-conjugated pH-responsive gold nanorods for combined photothermal therapy and chemotherapy of cancer. *Bioact Mater*. 2018;3(3):347–354. doi:10.1016/j.bioactmat.2018.05.003
18. Zhao X, Liu Y, Shao C, et al. Photoresponsive delivery microcarriers for tissue defects repair. *Adv Sci*. 2019;6(20):1901280. doi:10.1002/advs.201901280
19. Luo D, Carter KA, Miranda D, Lovell JF. Chemophototherapy: an emerging treatment option for solid tumors. *Adv Sci*. 2017;4(1):1600106. doi:10.1002/advs.201600106
20. Yang Y, Yun K, Li Y, et al. Self-assembled multifunctional polymeric micelles for tumor-specific bioimaging and synergistic chemo-phototherapy of cancer. *Int J Pharm*. 2021;602:120651. doi:10.1016/j.ijpharm.2021.120651
21. Cheng W, Nie J, Gao N, et al. A multifunctional nanoplatform against multidrug resistant cancer: merging the best of targeted chemo/gene/photothermal therapy. *Adv Funct Mater*. 2017;27(45):1704135. doi:10.1002/adfm.201704135
22. Jang B, Kwon H, Katila P, Lee SJ, Lee H. Dual delivery of biological therapeutics for multimodal and synergistic cancer therapies. *Adv Drug Delivery Rev*. 2016;98:113–133. doi:10.1016/j.addr.2015.10.023
23. Chen H, Zeng X, Tham HP, et al. NIR-light-activated combination therapy with a precise ratio of photosensitizer and prodrug using a host-guest strategy. *Angew Chem Int Ed*. 2019;58(23):7641–7646. doi:10.1002/anie.201900886
24. Lin Y-X, Wang Y, An H-W, et al. Peptide-based autophagic gene and cisplatin co-delivery systems enable improved chemotherapy resistance. *Nano Lett*. 2019;19(5):2968–2978. doi:10.1021/acs.nanolett.9b00083
25. Allen TM, Cullis PR. Liposomal drug delivery systems: from concept to clinical applications. *Adv Drug Delivery Rev*. 2013;65(1):36–48. doi:10.1016/j.addr.2012.09.037
26. Das M, Huang L. Liposomal nanostructures for drug delivery in gastrointestinal cancers. *J Pharmacol Exp Ther*. 2019;370(3):647–656. doi:10.1124/jpet.118.254797
27. Shi J, Kantoff PW, Wooster R, Farokhzad OC. Cancer nanomedicine: progress, challenges and opportunities. *Nat Rev Cancer*. 2017;17(1):20–37.
28. Kim HY, Kang M, Choo YW, et al. Immunomodulatory lipocomplex functionalized with photosensitizer-embedded cancer cell membrane inhibits tumor growth and metastasis. *Nano Lett*. 2019;19(8):5185–5193. doi:10.1021/acs.nanolett.9b01571
29. Liu X, Situ A, Kang Y, et al. Irinotecan delivery by lipid-coated mesoporous silica nanoparticles shows improved efficacy and safety over liposomes for pancreatic cancer. *ACS Nano*. 2016;10(2):2702–2715. doi:10.1021/acsnano.5b07781
30. Wang C, Wu B, Wu Y, Song X, Zhang S, Liu Z. Camouflaging nanoparticles with brain metastatic tumor cell membranes: a new strategy to traverse blood-brain barrier for imaging and therapy of brain tumors. *Adv Funct Mater*. 2020;30(14):1909369. doi:10.1002/adfm.201909369
31. Wu H, Jiang X, Li Y, et al. Engineering stem cell derived biomimetic vesicles for versatility and effective targeted delivery. *Adv Funct Mater*. 2020;30(49):2006169. doi:10.1002/adfm.202006169
32. Yang Q, Xiao Y, Yin Y, Li G, Peng J. Erythrocyte membrane-camouflaged IR780 and DTX coloading polymeric nanoparticles for imaging-guided cancer photo-chemo combination therapy. *Mol Pharm*. 2019;16(7):3208–3220. doi:10.1021/acs.molpharmaceut.9b00413
33. Rao L, Bu LL, Ma L, et al. Platelet-facilitated photothermal therapy of head and neck squamous cell carcinoma. *Angew Chem*. 2018;130(4):998–1003. doi:10.1002/ange.201709457
34. Zhang X, Cheng L, Lu Y, et al. A MXene-based bionic cascaded-enzyme nanoreactor for tumor phototherapy/enzyme dynamic therapy and hypoxia-activated chemotherapy. *Nano-Micro Lett*. 2022;14:1–21. doi:10.1007/s40820-021-00761-w
35. Xuan M, Shao J, Dai L, et al. Macrophage cell membrane camouflaged Au nanoshells for *in vivo* prolonged circulation life and enhanced cancer photothermal therapy. *ACS Appl Mater Interfaces*. 2016;8(15):9610–9618. doi:10.1021/acsami.6b00853
36. Yang Z, Gao D, Guo X, et al. Fighting immune cold and reprogramming immunosuppressive tumor microenvironment with red blood cell membrane-camouflaged nanobullets. *ACS Nano*. 2020;14(12):17442–17457. doi:10.1021/acsnano.0c07721
37. Zheng D, Yu P, Wei Z, Zhong C, Wu M, Liu X. RBC membrane camouflaged semiconducting polymer nanoparticles for near-infrared photoacoustic imaging and photothermal therapy. *Nano-Micro Lett*. 2020;12:1–17. doi:10.1007/s40820-020-00429-x
38. Zheng M, Zhao P, Luo Z, et al. Robust ICG theranostic nanoparticles for folate targeted cancer imaging and highly effective photothermal therapy. *ACS Appl Mater Interfaces*. 2014;6(9):6709–6716. doi:10.1021/am5004393
39. Zheng M, Yue C, Ma Y, et al. Single-step assembly of DOX/ICG loaded lipid-polymer nanoparticles for highly effective chemo-photothermal combination therapy. *ACS Nano*. 2013;7(3):2056–2067. doi:10.1021/nn400334y
40. Xu H-L, Shen B-X, Lin M-T, et al. Homing of ICG-loaded liposome inlaid with tumor cellular membrane to the homologous xenografts glioma eradicates the primary focus and prevents lung metastases through phototherapy. *Biomater Sci*. 2018;6(9):2410–2425. doi:10.1039/C8BM00604K
41. Al-Ahmady ZS, Al-Jamal WT, Bossche JV, et al. Lipid-peptide vesicle nanoscale hybrids for triggered drug release by mild hyperthermia *in vitro* and *in vivo*. *ACS Nano*. 2012;6(10):9335–9346. doi:10.1021/nn302148p
42. Dicheva BM, Hagen TLT, Li L, et al. Cationic thermosensitive liposomes: a novel dual targeted heat-triggered drug delivery approach for endothelial and tumor cells. *Nano Lett*. 2013;13(6):2324–2331. doi:10.1021/nl3014154
43. Xia Q, Zhang Y, Li Z, et al. Red blood cell membrane-camouflaged nanoparticles: a novel drug delivery system for antitumor application. *Acta Pharm Sin B*. 2019;9(4):675–689. doi:10.1016/j.apsb.2019.01.011
44. Hong C, Huizi S, Lianru Z, et al. Lipid insertion enables targeted functionalization of paclitaxel-loaded erythrocyte membrane nanosystem by tumor-penetrating bispecific recombinant protein. *Int J Nanomed*. 2018:5347–5359.
45. Zhang H. Erythrocytes in nanomedicine: an optimal blend of natural and synthetic materials. *Biomater Sci* 2016;4(7):1024–1031. doi:10.1039/C6BM00072J
46. Jung B, Vullev VI, Anvari B. Revisiting indocyanine green: effects of serum and physiological temperature on absorption and fluorescence characteristics. *IEEE J Sel Top Quantum Electron*. 2013;20(2):149–157. doi:10.1109/JSTQE.2013.2278674
47. Sibrian-Vazquez M, Escobedo JO, Lowry M, et al. Field effects induce bathochromic shifts in xanthene dyes. *J Am Chem Soc*. 2012;134(25):10502–10508. doi:10.1021/ja302445w

48. Li Z, Wang D, Xu M, et al. Fluorine-containing graphene quantum dots with a high singlet oxygen generation applied for photodynamic therapy. *J Mat Chem B*. 2020;8(13):2598–2606. doi:10.1039/C9TB02529D
49. Yu D, Zha Y, Zhong Z, et al. Improved detection of reactive oxygen species by DCFH-DA: new insight into self-amplification of fluorescence signal by light irradiation. *Sens Actuators B*. 2021;339:129878. doi:10.1016/j.snb.2021.129878
50. Jiang Z, Dong B, Chen B, et al. Multifunctional Au@ $mSiO_2$/rhodamine B isothiocyanate nanocomposites: cell imaging, photocontrolled drug release, and photothermal therapy for cancer cells. *Small*. 2013;9(4):604–612. doi:10.1002/smll.201201558
51. Stewart AF, Schütz G. Camptothecin-induced *in vivo* topoisomerase I cleavages in the transcriptionally active tyrosine aminotransferase gene. *Cell*. 1987;50(7):1109–1117. doi:10.1016/0092-8674(87)90177-2
52. Luo Z, Cai K, Hu Y, et al. Redox-responsive molecular nanoreservoirs for controlled intracellular anticancer drug delivery based on magnetic nanoparticles. *Adv Mater*. 2012;24(3):431–435. doi:10.1002/adma.201103458